Research Article Vol. 34, No. 16 / 10 Aug 2026 / Optics Express 28928
Optics EXPRESS

1-THz-to-mid-infrared field-resolved spectrometer driven by a Cr:ZnS oscillator

Daiki Okazaki,[1,2,5] Max Koch,[2,3] Mojtaba Aghakasiri,[2] Philipp Steinleitner,[2] Wolfgang Schweinberger,[3,4] Dionysios Potamianos,[3,4] Yang Gui,[2,3] Aleksandar Sebesta,[2,4] Behnam Jahedi Abbasvand,[3] Vipulkumar Bhaliya,[3] Shigeki Tokita,[1] Ferenc Krausz,[2,3,4] and Alexander Weigel[2,3,4,*]

[1]*Institute for Chemical Research, Kyoto University, Gokasho, Uji, 611-0011 Kyoto, Japan*
[2]*Max-Planck-Institute of Quantum Optics, Hans-Kopfermann-Str. 1, 85748 Garching, Germany*
[3]*Ludwig-Maximilians-Universität München, Am Coulombwall 1, 85748 Garching, Germany*
[4]*Center for Molecular Fingerprinting, Frontiers Foundation, 1093 Budapest, Czuczor utca 2-10, Hungary*
[5]*okazaki@laser.kuicr.kyoto-u.ac.jp*
[*]*alexander.weigel@mpq.mpg.de*

Abstract: The mid-infrared (MIR) and terahertz (THz) spectral regions provide complementary insights into molecular structure and dynamics, with the MIR probing intramolecular vibrations and the THz region probing intermolecular interactions, lattice vibrations, and collective motions. Comprehensive molecular spectroscopy therefore requires broadband, gap-free access spanning both regimes. Here, we present a compact platform for broadband THz generation and detection driven by 2.3-μm-centered, near-single-cycle (13-fs) pulses from a mode-locked Cr:ZnS oscillator. Leveraging the wide transparency windows and large nonlinear coefficients of organic crystals, we achieve efficient THz generation up to 39 THz with pump energies of only a few nanojoules, and observe no degradation over months of operation. Using a pump pulse energy of 3.0 nJ, a THz output of 1.1 pJ was achieved. Highly reproducible THz waveform generation and detection with a time-domain peak-to-peak electric-field signal-to-noise ratio exceeding 2000 (35 min acquisition with 8.6 kHz modulation) was demonstrated over 10 hours. As an application, we demonstrate broadband absorption spectroscopy of polymer films, resolving characteristic resonances across the 1–30 THz range. These results establish a robust and efficient approach for field-resolved molecular spectroscopy across the THz-to-MIR domain, based on newly emerged few-cycle mode-locked Cr:ZnS oscillator technology, paving the way toward ultra-broadband coverage from 1–100 THz with table-top systems.

1. Introduction

The mid-infrared (MIR) spectral region contains abundant information on the resonant frequencies of intramolecular vibrations and has long been referred to as the "molecular fingerprint region", where extensive studies have enabled the identification of molecular species, functional groups, and specific chemical bonds [1,2]. The molecular sensitivity of infrared spectroscopy also makes it suitable for providing a fingerprint of the molecular composition of biologically relevant samples such as human blood serum or plasma, with recent applications in disease detection [3,4]. Complementary to the MIR, the terahertz (THz) region reveals absorption features that originate predominantly from collective molecular motions, lattice vibrations, and intermolecular interactions, thereby providing insights into tertiary and quaternary structures of proteins, phonon absorptions, the surrounding environment of molecules, and hydrogen-bonding networks [5–7]. Extending the MIR spectral range into the THz regime therefore adds complementary

#596193 https://doi.org/10.1364/OE.596193
Journal © 2026 Received 23 Feb 2026; revised 8 Jun 2026; accepted 8 Jun 2026; published 28 Jul 2026

Optics EXPRESS

structure-sensitive information that can be essential for improving future diagnostic performance of approaches such as fingerprint-pattern-based disease detection.

The information content of spectroscopic measurements in the MIR and THz regimes largely depends on the accessible resonant vibrations and motions, and thus the spectral bandwidth. Traditional Fourier-transform infrared (FTIR) spectroscopy employs incoherent thermal sources and provides broadband spectral coverage, but the inherently low brightness, poor directionality, and low spatial coherence of thermal radiation restrict measurement sensitivity, limiting the variety of its applications. Laser-based MIR and THz spectroscopy overcomes the limitations of thermal sources, providing bright, directional temporally and spatially coherent MIR and THz radiation [8]. When combined with time-domain electric-field-resolved detection via electro-optic sampling (EOS), laser-based MIR spectroscopy has demonstrated improved limit of detecting small changes in molecular composition over FTIR [9].

The narrower emission and detection bandwidths of laser-based systems compared with thermal sources have long been a major limiting factor for spectroscopic applications. However, recent advances in ultrafast laser technology have enabled the development of broadband coherent sources across the MIR region. In particular, mode-locked Cr:ZnS oscillators have emerged as efficient and stable drivers in the 2–3 μm spectral region [10–16]. When combined with advanced $\chi^{(2)}$-nonlinear materials such as zinc germanium phosphide (ZGP) or gallium selenide (GaSe), these oscillators enable intrapulse difference-frequency generation (IPDFG), yielding super-octave-spanning MIR radiation from 3 to 12 μm (100–25 THz) [17] or from 9 to 22 μm (33–13 THz) [18]. Such MIR supercontinuum sources, operating at megahertz or gigahertz repetition rates, can provide spectral brightness surpassing that of synchrotron-based infrared beamlines [8,19]. Furthermore, their intrinsic waveform stability allows field-resolved detection via electro-optic sampling, achieving a high dynamic range and quantum-limited sensitivity with ultra-rapid data acquisition [9,20].

While IPDFG in combination with EOS detection has been established as a powerful platform for MIR molecular spectroscopy, extending broadband coverage seamlessly into the THz regime remains a major challenge. Conventional approaches to THz generation based on nonlinear semiconductor crystals are limited by Reststrahlen bands — spectral regions of strong phonon-induced absorption and dispersion — which introduce serious spectral gaps [18]. At the same time, in kilohertz, millijoule-class laser systems, these bandwidth limitations have been substantially overcome by broadband THz generation and detection schemes such as THz air photonics and solid-state biased detection, enabling broadband field-resolved spectroscopy over the 1–30 THz range [21,22].

Compared with the method above, organic crystals do not exhibit strong Reststrahlen absorption bands, and possess large nonlinear optical coefficients. As a result, efficient broadband generation has been achieved even with nanojoule-level pump pulses [23–29]. While broadband oscillator-driven THz sources at high repetition rates based on an Er-fiber laser have already been demonstrated [30], there remains a need for compact field-resolved spectroscopic platforms that integrate both THz generation and detection with broad and practically usable coverage spanning the THz-to-MIR range.

In this work, we report a novel approach to high-repetition-rate THz generation and detection based on a mode-locked Cr:ZnS oscillator and organic nonlinear crystals which enables efficient THz generation covering the 1–39 THz spectral range. Our oscillator-based platform provides near-single-cycle pulses at 2.3 μm, which is advantageous for broadband field-resolved spectroscopy at the system level. The near-single-cycle pulses are essential for multi-octave THz generation, while the same wavelength range is also well suited to broadband electro-optic detection with ZnTe. In addition, the platform operates at megahertz repetition rates, offering distinct advantages in rapid signal averaging. Using this platform, we demonstrate THz generation driven by either the direct 33-fs output of the Cr:ZnS oscillator or near-single-cycle (13-fs, 1.7-cycle) pulses obtained by

Optics EXPRESS

nonlinear post-compression in rutile TiO_2 [31]. We compare the THz output characteristics of the two excitation regimes. Importantly, the near-single-cycle driver is a prerequisite for achieving the multi-octave coverage, whereas the 33-fs excitation yields a narrower spectrum. We also demonstrate the spectroscopic utility of our scheme by measuring molecular absorption features across the THz and MIR regions in semiconductor and polymer samples.

Our results extend the previously reported MIR continuum generation (3–12 μm, 25–100 THz) [17] into the THz regime (10–300 μm, 1–30 THz), establishing an ultra-broadband, field-resolved spectroscopic approach that spans the full 1–100 THz range with a near-single-cycle Cr:ZnS oscillator platform [31]. This seamless coverage opens the door to data-driven discovery: leveraging rapidly growing machine-learning methodologies, one can mine previously inaccessible correlations among disparate absorption bands to extract new molecular insights.

2. Experimental setup

2.1. Layout of the THz-to-MIR field-resolved spectrometer

A schematic of the experimental setup for ultrabroadband THz-to-MIR field-resolved spectroscopy is shown in Fig. 1(a). A home-developed Kerr-lens mode-locked Cr:ZnS oscillator [31,32] with a 23 MHz repetition rate serves as the driving laser, delivering close-to-Fourier-transform-limited pulses centered at 2.3 μm with a duration of 33 fs and an average output power of 520 mW. Figures 1(b) and (c) (upper panels) show the output pulse spectrum, as well as the temporal pulse structure and phase retrieved from frequency-resolved optical gating (FROG) measurements. Optionally, the direct laser output pulses are further spectrally broadened in a (001)-oriented, 500-μm-thick TiO_2 plate, and then temporally compressed by a pair of dispersive mirrors [31,33], yielding 300 mW of 12.7-fs pulses, corresponding to 1.7 optical cycles at a carrier wavelength of 2.3 μm. The spectrum and FROG results of the post-compressed pulses are shown in Fig. 1(b) and (c) (lower panels). The output beam of the Cr:ZnS oscillator (direct output or post-compressed) is split by a 0.35-mm-thick wedged ZnS plate: the reflection from the first surface is used as the gating beam for detection, while the internal reflection from the second surface is used to monitor the oscillator output. The transmitted beam is used to drive THz generation. To avoid damage to the organic crystals, it is attenuated to 35 mW before the crystals using a combination of an achromatic half-wave-plate (B. Halle) and a polarizer (WP25M-UB1, Thorlabs).

For THz generation, the driving pulses are focused using a 15-mm-focal-length protected-silver off-axis parabolic mirror to a beam diameter of 15 μm ($1/e^2$). The emitter crystal was positioned in the vicinity of this focus and then fine-tuned to maximize the detected THz signal. The THz driving beam is modulated at 8.6 kHz with a 50 % duty cycle by a mechanical chopper (3502, Newport) for downstream lock-in detection. The THz power measurements were performed with a Golay cell (GC-1P, TYDEX) at a chopping frequency of 10 Hz and the pump beam was attenuated to prevent saturation of the detector. The results were then scaled to the full-power conditions according to the change in the square of the EOS peak-to-peak signals (see Supplement 1).

The THz beam is collimated after generation with a 50.8-mm-focal-length unprotected-gold parabolic mirror. To minimize losses, this and all downstream parabolic mirrors in the THz beam path have a diameter of 3 inches. After collimation, a second pair of parabolic mirrors (f = 228.6 mm) forms an intermediate focus, near which the sample for spectroscopic measurements is placed. The recollimated beam is then focused with a 50.8-mm-focal-length parabolic mirror into the electro-optic (EO) crystal for electric-field-resolved detection. Either (110)-cut zinc telluride (ZnTe; 50- or 100-μm thick) or (110)-cut gallium phosphide (GaP; 100-μm thick) was used as the EO crystal.

The gate beam for EOS detection is rotated to s-polarization (perpendicular to the page in Fig. 1(a), perpendicular to the THz-beam polarization by using a periscope. When using the direct oscillator output, instead, the gate polarization is rotated by an achromatic half-wave plate (B. Halle) instead of using a periscope. The gate pulses are combined with the THz radiation by

Optics EXPRESS

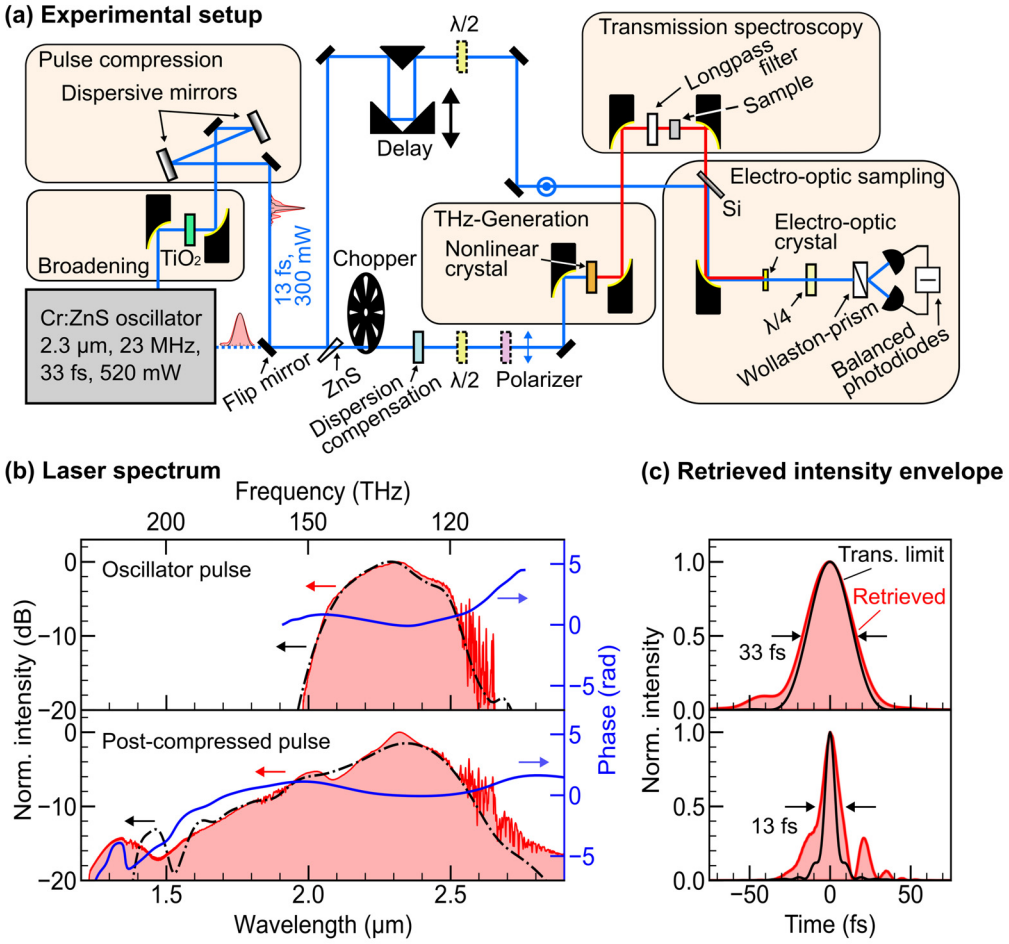

Fig. 1. (a) Schematic of the field-resolved spectrometer based on a home-built mode-locked Cr:ZnS oscillator. $\lambda/2$: optional half-wave plate; $\lambda/4$: quarter-wave plate. (b) Upper panel: Power spectrum (red) and spectral phase (blue) of the oscillator output; the black dashed curve shows the power spectrum retrieved from FROG. Lower panel: the same for the post-compressed pulse. (c) Upper panel: Normalized temporal intensity of the oscillator output; the black dashed curve shows the calculated Fourier-transform-limited pulse. Lower panel: the same for the post-compressed pulse.

reflection from a 3-inch-diameter, 1-mm-thick high-resistivity float-zone silicon wafer (HRFZ-Si, TYDEX) in the THz beam path. After beam combination, the gate pulses are focused collinearly with the THz pulses into the EO crystal.

The electro-optically induced polarization change of the gate pulses is analyzed using an ellipsometry setup consisting of an achromatic quarter-wave plate (SAQWP05M-1700, Thorlabs), a Wollaston prism (WPA10, Thorlabs), and a home-built balanced photodetector with extended InGaAs PIN photodiodes (G12183-103K, Hamamatsu Photonics) and a built-in transimpedance amplifier with a gain of 5.1 kV/A. The differential signal is fed to a lock-in amplifier (MFLI or HF2LI, Zurich Instruments) that is synchronized to the chopping frequency and operated with a 3-ms integration time constant. Time-domain THz waveforms are recorded by scanning a voice-coil motorized stage (V-528.1AA, Physik Instrumente) in the gate beam path at a velocity of 100 μm/s, while monitoring the position precisely with an interferometric delay-tracking module

Optics EXPRESS

(PICOSCALE Interferometer, SmartAct). The stage velocity was chosen as the fastest value that does not cause attenuation of the highest detected frequency components under the present lock-in-based acquisition conditions. For all THz measurements (except for measurements of MIR generation from ZGP), the THz beam path was purged with nitrogen to keep the humidity below 3 %. Each trace shown in the results section represents an average of 50 individual full-delay scans, unless stated otherwise.

2.2. Terahertz detection with 2.3-μm gate pulses

Before the spectral analysis of THz generation, we first study the characteristics of our EOS detection at 2.3 μm. Table 1 summarizes the bandgap energies, phonon absorption frequencies, nonlinear coefficients at 800 nm, and refractive indices of typical EO crystals used for THz detection [34–47]. Due to their high nonlinear coefficients, favorable phase-matching conditions (see below), and availability, we found ZnTe and GaP the most suitable crystals for EOS detection.

Table 1. Comparison of material parameters relevant to EOS [34–47]. E_g, bandgap; f_0^{THz}, phonon resonance frequency; d_{eff}, effective nonlinear coefficient; $n_{2.3\mu m}$, group index at 2.3 μm; n_{1THz}, refractive index at 1 THz. In GaSe, (o) and (e) denote the ordinary and extraordinary axes.

	GaSe	ZnTe	GaP	GaAs	CdTe
E_g (eV)	2.0 [35]	2.3 [41]	2.3 [40]	1.4 [40]	1.5 [50]
f_0^{THz} (THz)	6.4 [45]	5.3 [36]	11 [39]	8.1 [39]	4.2 [44]
d_{eff} (pm/V) [34]	28	69	25	66	82
$n_{2.3\mu m}$	2.77 (o) [47] 2.44 (e) [47]	2.74 [37]	3.06 [42]	3.40 [46]	2.75 [37]
n_{1THz}	3.27 (o) [45] 2.49 (e) [45]	3.17 [36]	3.34 [39]	3.59 [39]	3.24 [44]

Organic crystals have also attracted considerable attention for broadband THz detection owing to their large electro-optic coefficients and broad detection bandwidths [28–49]. In this work, however, we employed ZnTe and GaP in order to use a robust and well-established EOS geometry based on isotropic semiconductor crystals. The implementation of organic EO crystals, which requires additional consideration of birefringence, polarization orientation, and calibration, remains an important future extension of the present spectroscopic platform.

Calculated transfer functions for EOS detection [51] are compared in Figs. 2(a)–(c) for different EO crystals with gate pulses centered at 2.3 μm (our case, shown in red) and at 0.8 and 1.15 μm, corresponding to typical Ti:sapphire and second-harmonic-generation (SHG) gating conditions for Cr:ZnS laser systems (see Supplement 1). Pronounced features around 5 THz for ZnTe and 11 THz for GaP arise from phonon absorption. At frequencies below the phonon-absorption frequency, THz radiation experiences normal dispersion; above it, anomalous dispersion. Periodic gaps in the transfer functions originate from phase mismatch between the THz and gate pulses in the EO crystal, with a periodicity that depends on the crystal thickness. Strikingly, phase matching becomes more favorable as the gate wavelength increases. At a gate wavelength of 2.3 μm, the phase mismatch in ZnTe is nearly the same in the normal and anomalous dispersion regions near the phonon resonance. This results in a relatively constant coherence length of about 100 μm and, correspondingly, a flat detection transfer function across a broad frequency range for EOS, for both 50- and 100-μm-thick ZnTe crystals (Fig. 2(a) and (b), red curves). At a gate wavelength of 2.3 μm and owing to its large nonlinear coefficient (69 pm/V), ZnTe is an ideal crystal for efficient, broadband EOS detection of THz pulses at frequencies below 4 THz and above 8 THz. For gapless detection below 10 THz, GaP is more suitable, owing to its higher phonon absorption frequency (see Fig. 2(c)). This comes at the expense of a much lower

Optics EXPRESS

nonlinear coefficient of 25 pm/V and less favorable phase matching at frequencies above 10 THz, compared with ZnTe. Based on these considerations, and taking into account crystal availability, we employed both ZnTe and GaP for EOS in our experiments to investigate the THz-waveforms over the full generation window.

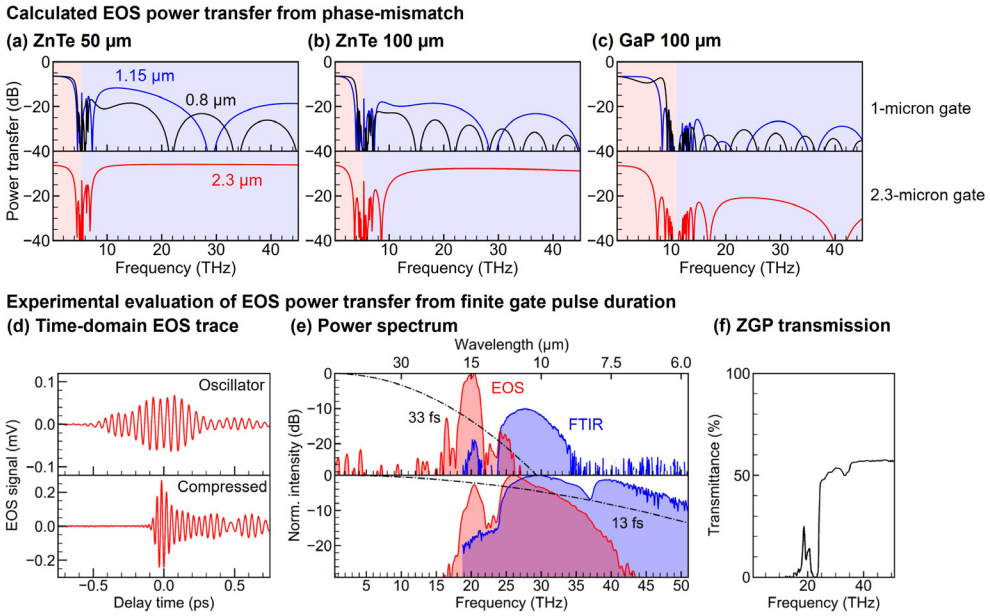

Fig. 2. Calculated EOS power transfer for (a) 50-μm-thick ZnTe, (b) 100-μm-thick ZnTe, and (c) 100-μm-thick GaP. Upper panels: gate wavelengths of 0.8 μm (black) and 1.15 μm (blue). Lower panels: a 2.3 μm gate is used (red). Red and blue shading represent the normal and anomalous dispersion regions, respectively. (d) Measured EOS trace and (e) corresponding power spectrum (red) for ZGP, detected with a 100-μm-thick ZnTe crystal. The upper and lower panels correspond to measurements with the oscillator pulse and the post-compressed pulse, respectively. The blue curves in (e) show spectra measured with an FTIR spectrometer, which has a long-wavelength cutoff at 16 μm. Black dashed curves indicate the power-transfer function due to the finite gate-pulse duration. (f) Transmission spectrum of ZGP. The data is digitized from Ref. [53].

The high-frequency limit of our EOS bandwidth is determined, in this experiment, primarily by the gate pulse duration. To characterize the detection bandwidth using a 100-μm-thick ZnTe crystal, we employed IPDFG in a 1-mm-thick ZGP crystal ($\theta = 51°$, $\phi = 0°$) as a broadband MIR or high-frequency THz source [17]. Figure 2(d) shows EOS time-domain traces obtained using the direct 33-fs oscillator output and the post-compressed 13-fs pulses, used both for driving IPDFG and for gating the detection. The corresponding power spectra, obtained by Fourier transforming the measured EOS traces, are shown in Fig. 2(e) (red), alongside spectra measured with a Fourier transform infrared spectrometer (FTIR Rocket 2-16, ARCoptix, spectral resolution of 2 cm^{-1}; blue). In the same figure, we also plot the calculated detection transfer functions based on analytical models (black dashed) [52].

A comparison of the power spectra obtained from EOS and FTIR measurements shows that the high-frequency components are attenuated in EOS detection. The calculated detection transfer function reproduces the general trend that the high-frequency cutoff redshifts with increasing gate-pulse duration, as shown in Fig. 2(e). With 13-fs driving and gate pulses, spectral components up to ca. 40 THz can be observed. The observed spectral cutoff with the compressed

Optics EXPRESS

pulses occurs at a lower frequency than the analytical estimate. This discrepancy can be explained by an effectively longer pulse duration than 13 fs inside the ZnTe crystal due to dispersion effects. As previously shown, further shortening of the gate-pulse duration can extend the electro-optic sampling with GaSe up to 100 THz (3 μm) [17]. In this study, we focus on the low-frequency spectral range below and around the ZGP cutoff. Figure 2(f) shows the ZGP transmission spectrum. Phonon absorption around 23 THz sets the lower frequency limit to the spectral coverage of pulses generated by IPDFG in ZGP. Transmission remains weak around 20 THz, but the low-frequency THz regime is not accessible using ZGP [53]. The 40-THz cut-off of our ZnTe-based EOS detection with 13-fs pulses extends well into the ZGP transparency regime, and is therefore suitable to achieve our experimental goal of seamlessly extending the spectral coverage achieved previously with ZGP further into the low-THz regime.

3. Results and discussion

3.1. Terahertz generation from organic crystals pumped by 2.3-μm pulses

In this study, several organic crystals on 1-mm-thick sapphire substrates (Swiss Terahertz) were employed for broadband THz generation via optical rectification. Figure 3 shows the calculated coherence lengths for the organic crystals used in this work:

DAST — 4-N,N-dimethylamino-4'-N'-methylstilbazolium tosylate,
DSTMS — 4-N,N-dimethylamino-4'-N'-methylstilbazolium 2,4,6-trimethylbenzenesulfonate,
OH-1 — 2-(3-(4-hydroxystyryl)-5,5-dimethylcyclohex-2-enylidene) malononitrile.

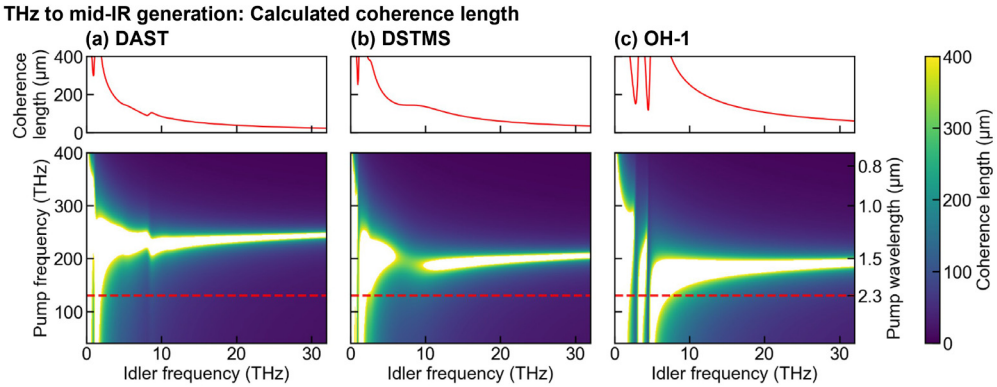

Fig. 3. Calculated coherence lengths for (a) DAST, (b) DSTMS, and (c) OH-1, depending on both pump and idler frequencies (2D maps), together with the coherence lengths at our pump frequency of 130 THz (2.3 μm, dashed red line), shown in the panels above.

The refractive indices [24] were obtained by extrapolation for excitation frequencies below 150 THz (i.e., $\lambda > 2$ μm) and for idler frequencies above 10 THz (i.e., $\lambda < 30$ μm). Therefore, the calculations may not capture variations in the refractive index due to absorption bands in these regions.

Phase-matching conditions of organic crystals have typically been optimized for near-infrared wavelengths of 1.3–1.5 μm. Therefore, synthesizing organic crystals optimized for excitation at 2.3 μm is highly desirable in future. For our pump frequency and the available crystals, the curves indicate that broadest phase matching is expected for crystal thicknesses below 100 μm, which could not be obtained by us at the time of these experiments. In this work, we therefore selected the thinnest commercially available crystals: 200-μm-thick DAST, 280-μm-thick DSTMS, and 380-μm-thick OH-1. Comparison of THz generation with the 200-μm-thick DAST crystal and

Optics EXPRESS

an even thicker crystal (440 μm, see Supplement 1) confirms that thinner organic crystals deliver superior performance in terms of signal strength and spectral bandwidth at our pump frequency.

Time-domain EOS traces and corresponding power spectra obtained from these organic crystals are shown in Fig. 4. As before, the results obtained with the direct 33-fs oscillator output (blue) and with the post-compressed 13-fs pulses are compared. In both cases, similar spectra and intensities are obtained in the low-frequency regime, whereas the high-frequency components are strongly enhanced with the 1.7-cycle, 13-fs driving and gate pulses. As a result, with compressed pulses, the peak-to-peak amplitude of the temporal signal increases by approximately one order of magnitude. As shown in Fig. 4(a) all three crystals, DAST, DSTMS, and OH-1, yield similar maximum time-domain signal levels, with DAST showing the strongest signal.

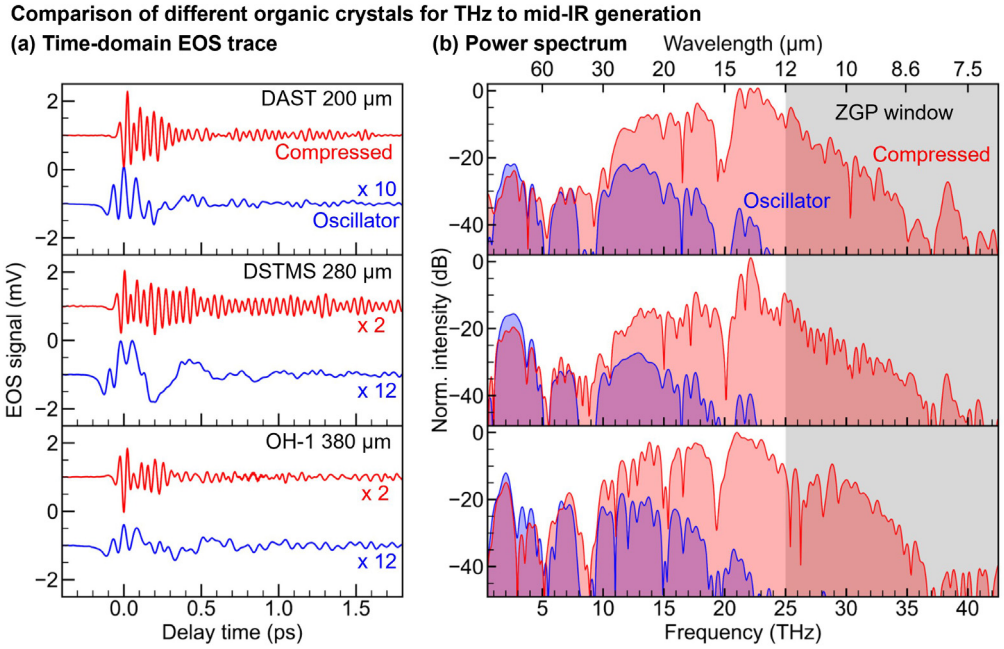

Fig. 4. (a) Measured EOS traces and (b) corresponding power spectra for the organic crystals, detected with a (110)-cut ZnTe crystal (t = 100 μm). The upper, middle, and lower panels correspond to measurements with DAST (t = 200 μm), DSTMS (t = 280 μm), and OH-1 (t = 380 μm), respectively. Red and blue curves denote measurements with post-compressed pulse and the oscillator output, respectively. In (a), each EOS trace is scaled for better comparison. In (b), each spectrum is normalized to the maximum spectral component for each crystal measured with the post-compressed pulse. The dark-shaded area marks the region where ZGP generates MIR components.

The overall spectral shapes shown in Fig. 4(b), obtained by Fourier transforming the EOS time-domain traces, are similar across all organic crystals. The spectra extend continuously to 30 THz at the -20 dB level, and are thus limited by the generation process, not by EOS detection. The spectral intensity is reduced near 6 THz due to phonon absorption in the ZnTe EO crystal. In addition, absorption-line features are observed that are characteristic of the organic crystals' absorption resonances and lead, in the time domain, to corresponding long-lived oscillations in the wake of the main pulses. In the spectral domain, DAST shows slight advantages for THz generation over the other organic crystals, with spectral components extending to 39 THz at the -40 dB level.

Optics EXPRESS

Our results demonstrate that the spectral range accessible by IPDFG of ultrashort pulses from Cr:ZnS oscillators in semiconductor crystals such as ZGP (dark-shaded area in Fig. 4) can be continuously extended by THz generation in organic crystals to the 1-THz regime. For the subsequent experiments, we used DAST for THz generation, driven by our 1.7-cycle, 13-fs pulses from the post-compressed Cr:ZnS oscillator output.

The optimized EOS trace, combining the most suitable conditions for ultra-broadband THz generation and EOS detection, is shown together with the corresponding power spectrum in Fig. 5. For THz generation, a 200-μm-thick DAST crystal was used, and for EO detection a 50-μm-thick ZnTe crystal was employed to suppress the effects of phonon absorption and phase mismatch in ZnTe around 5.3 THz, while sacrificing the signal strength in evaluated time domain. As shown in Fig. 5(a), the signal-to-noise ratio (SNR) in the time domain is 250 for a single trace (21 seconds of acquisition) and increases to 2036 when 100 traces are averaged (35 minutes of acquisition), and reaches 2146, when in post-processing a Fourier-low-pass filter with a cutoff frequency of 45 THz is applied.

The output power of the generated THz-to-MIR pulses was measured with a Golay cell (GC-1P, TYDEX) at a chopping frequency of 10 Hz. The excitation power had to be reduced for this measurement from 35 mW (3.0 nJ) to 17 mW (1.5 nJ) to avoid detector saturation. Under these conditions, 3.2 μW (0.27 pJ) were measured, corresponding to a conversion efficiency of 0.019%. Residual pump light was evaluated by repeating the measurement with the crystal rotated by 90°; the resulting background signal, corresponding to approximately 10% of the total detector output, was subtracted. Thus, the output power for the 35 mW pumping condition is calculated from EOS signal linearity as 14 μW (1.1 pJ), corresponding to a conversion efficiency of 0.040%.

The EOS power spectrum shown in Fig. 5(b), extends from 1 to 39 THz. The spectral dip at 5 THz originates from absorption in ZnTe, whereas the dip near 8 THz is caused by phase mismatch in ZnTe. Additional fine dips, indicated by the black dashed line in Fig. 5(b), are attributed to absorption in DAST (black dashed curve) [24,54]. Shallow fringes with nearly equal spacing are due to surface reflections inside the ZnTe crystal.

The high-frequency part of the spectrum was additionally measured with an FTIR spectrometer (blue curve in Fig. 5(b)). The two spectra agree, taking into account the high-frequency roll-off caused by the limited gate-pulse duration in EOS. This consistency confirms that our THz generation and detection scheme extends up to 39 THz and that spectral shapes are reliably reproduced by our EOS measurements. Furthermore, we confirm the absence of a cascaded process, since no higher-frequency components are observed in the FTIR measurements, and conclude that THz generation is limited to frequencies below 40 THz.

The pump-power dependence of the EOS signal was separately investigated. Figure 5(c) shows the dependence of the relative EOS peak-to-peak amplitude with pump power, together with a linear fit. The linear dependency of the THz electric field corresponds to a square dependence of the THz power with pump power and indicates that THz generation is dominated by pure 2nd-order nonlinearity. Both time-domain EOS waveforms (Fig. 5(d)) and EOS power spectra (Fig. 5(e)) remain unchanged in shape with pump power. Taken together, we conclude that THz generation driven by our 2.3-μm pulses in a 200-μm-thick DAST crystal is dominated by pure IPDFG, without any cascading effects.

The long-term stability of DAST as a THz-generation crystal was evaluated by performing continuous measurements over 11 hours, yielding a total of 3518 traces. As seen in Fig. 6(a), no degradation of the peak-to-peak electric-field amplitude was observed, and stable THz waveforms were recorded over the entire measurement period. The reproducibility of the THz waveforms is further evidence for the absence of cascading effects, which would render the waveform dependent on carrier-envelope-phase drifts of the unstabilized Cr:ZnS oscillator [17]. Correspondingly, the power spectra obtained by Fourier transformation, shown in Fig. 6(b), also remained unchanged in shape over the entire 11-hour measurement period. In addition, during intermittent use over a

Optics EXPRESS

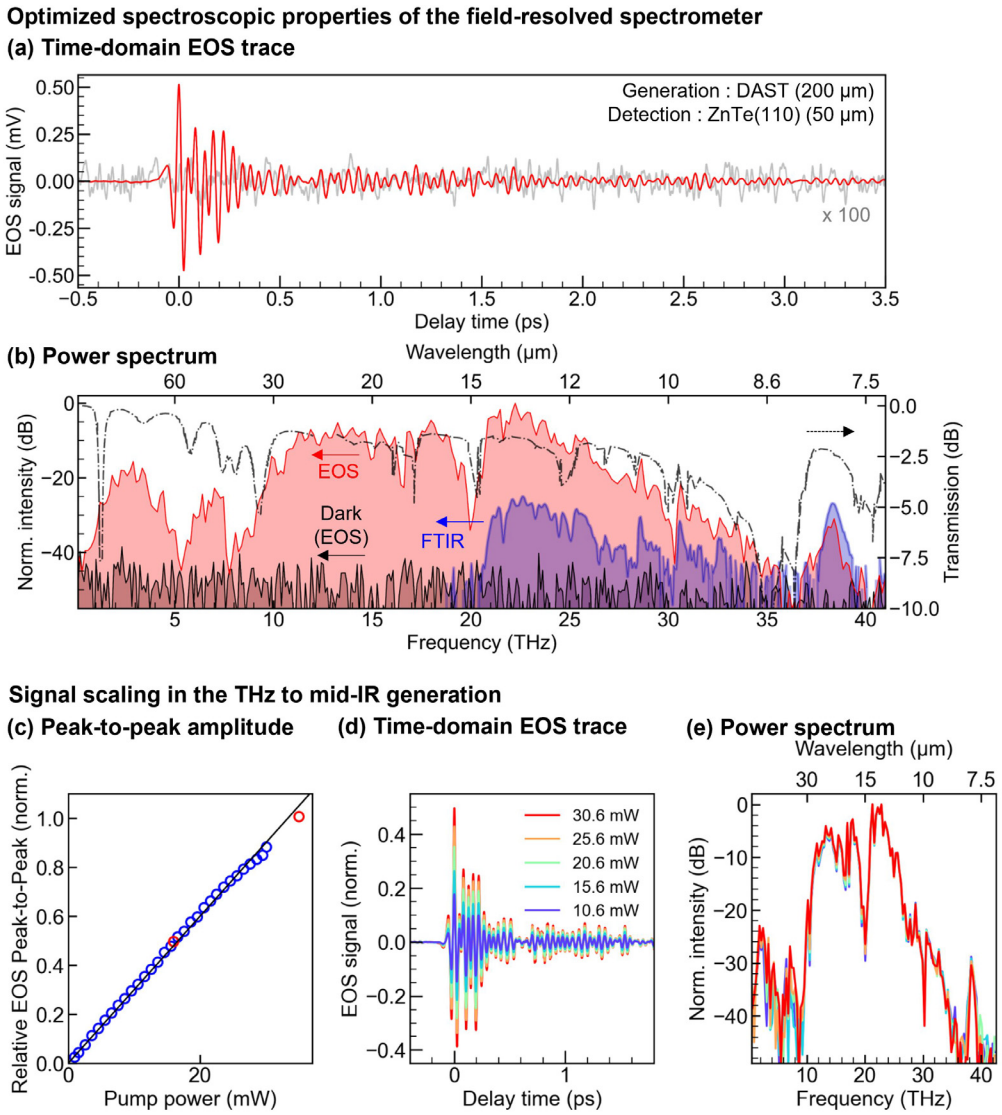

Fig. 5. (a) Measured EOS trace from DAST (t = 200 μm, red) detected with (110)-cut ZnTe (t = 50 μm). Gray: averaged dark signal, scaled by a factor of 100. (b) Corresponding power spectrum (red) and averaged dark spectrum (black). The blue curve corresponds to the same power spectrum measured with an FTIR spectrometer, which has a long-wavelength cutoff at 16 μm. The black dashed line indicates the transmission spectrum of DAST [24,54]. (c) Measured EOS peak-to-peak amplitude as a function of pump power, relative to the value at 35 mW. Red and blue measurement data were recorded with a realignment of the experimental setup in between. The line is a linear fit to the experimental data. (d) Measured EOS waveforms and (e) corresponding power spectra of THz pulses at different pump power levels.

Optics EXPRESS

period of six months, no significant signal degradation has been observed to date. Our results confirm that the spectroscopic system based on THz generation in DAST and EOS detection in ZnTe continuously covers the spectral range from 1 to 39 THz without any signs of degradation or drift over hours or even months of operation, making it highly suitable for spectroscopic applications.

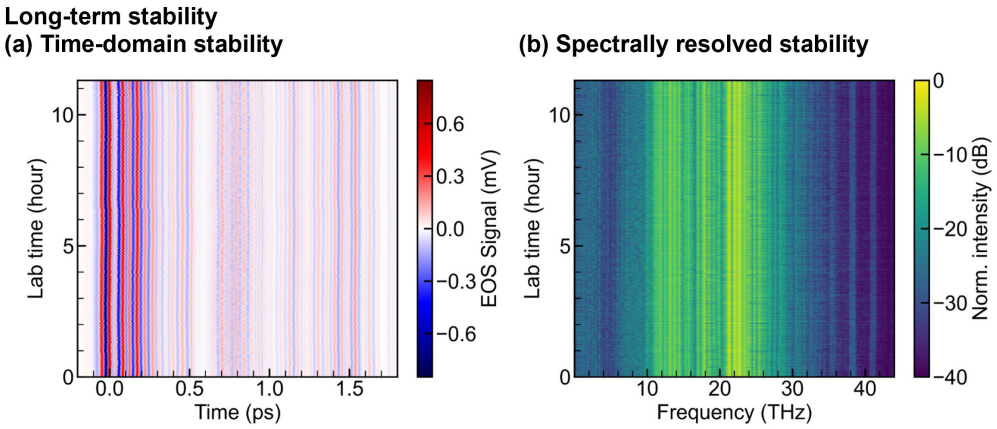

Fig. 6. (a) Long-term stability of the EOS trace for DAST (t = 200 μm) detected with (110)-cut ZnTe (t = 50 μm). (b) Long-term stability of the corresponding power spectrum.

4. Spectroscopic measurements

Finally, we demonstrate transmission-based absorption measurements of solid samples (Fig. 7) with our broadband time-domain THz spectrometer operated with the post-compressed, 1.7-cycle pulses. As samples, we investigated a 100-μm-thick ZnTe crystal, a 380-μm-thick polyethylene (PE)-based infrared film (#32-807, Edmund Optics), and a 150-μm-thick polytetrafluoroethylene (PTFE) film. For the transmission measurement of ZnTe, a 100-μm-thick GaP crystal was employed for EO detection. The measurement characteristics of EOS using GaP as the detection crystal are discussed in Supplement 1. The measured time-domain traces are averages of 100 measurements, with the shaded area consisting of the superposition of the individual single-shot traces. The absorbance spectra obtained by Fourier-transform analysis of the time-domain EOS traces demonstrate continuous spectral coverage from the THz to the mid-infrared regime, with spikes in the standard deviations (red shading) corresponding to spectral dips in the source spectrum.

EOS traces and the absorbance spectrum of a 100-μm-thick ZnTe sample are shown in Figs. 7(a) and 7(d), respectively. Time-domain traces with the ZnTe sample were scaled by a factor of 0.74 due to strong surface reflections. As a result, the dynamic range of the measurement is limited, and the maximum observable absorbance is restricted to a value of 2. Nevertheless, the data show strong absorption around 5 THz, corresponding to the Reststrahlen band of ZnTe reported in the literature [39].

Results for the PE-based infrared film are shown in Figs. 7(b) and 7(e). In the range of 12–30 THz, the measured spectrum agrees with the reference spectrum obtained from FTIR measurements (Vertex 70, Bruker Optics GmbH, spectral resolution of 2 cm^{-1}). Within this range, we observe a broad absorption feature centered at 14 THz and a sharp absorption peak at 21 THz. At 21 THz, the spectrum lies in the region where the generated THz radiation has the highest power, enabling us to resolve a strong CH_2 rocking-mode absorption peak [55] with an absorbance of 3.5.

Optics EXPRESS

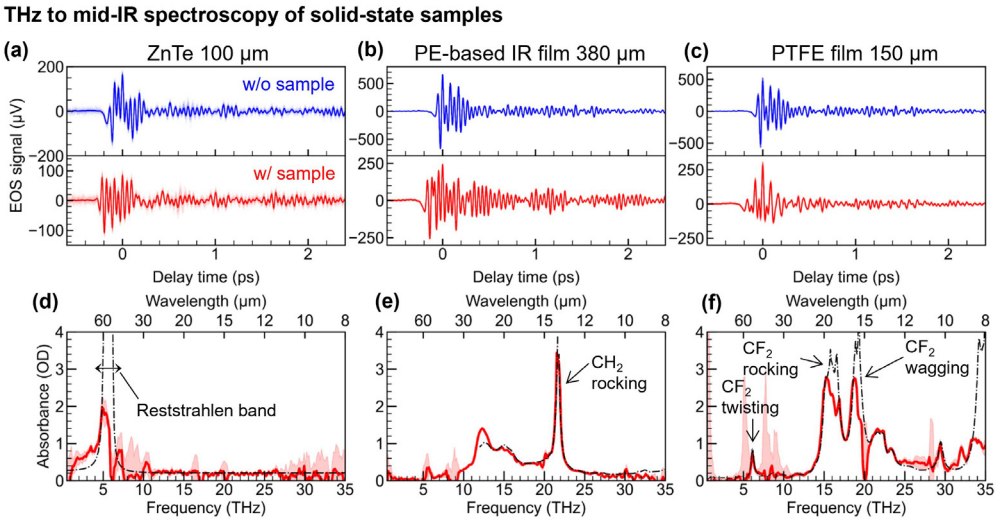

Fig. 7. (a)–(c) Measured EOS traces without (blue) and with (red) the sample: (a) ZnTe, (b) PE-based IR film, and (c) PTFE film. The blue and red shaded areas show the spread of all measurement traces for each case. (d)–(f) Extracted absorbance spectra for (d) ZnTe, (e) PE-based IR film, and (f) PTFE film. Black dashed curves represent the reference spectra. The red shaded area corresponds to the 1σ standard deviation.

Results for the PTFE film are shown in Figs. 7(c) and 7(f). The absorption peak at 6 THz, attributed to the CF_2 twisting mode, is in agreement with values reported in the literature [22,56]. Although the dynamic range was limited, as in the ZnTe measurement, strong absorption features originating from CF_2 rocking at 16 THz and wagging at 19 THz were resolved [57], consistent with the absorbance spectrum measured by our FTIR. A peak observed at 29 THz, also confirmed by our FTIR measurements, is likely due to impurities and is assigned to C–Cl stretching in polychlorotrifluoroethylene [57].

These results demonstrate broadband transmission-based absorption spectroscopy spanning from the terahertz to the infrared region, with spectral coverage from 1 to above 30 THz. This spectral range is already well suited to condensed-phase THz spectroscopy, where the relevant vibrational features are typically much broader than narrow gas-phase lines and can therefore be captured within the present few-picosecond delay window. Since THz generation in our scheme requires only about 3 nJ of pump energy, the approach can be readily integrated with previously demonstrated ZGP-based spectroscopic systems [17]. Such a combination will enable field-resolved THz-to-MIR spectroscopy covering the entire 1–100 THz range using a single Cr:ZnS oscillator platform.

5. Summary

In this work, we demonstrated broadband THz generation and detection using 1.7-cycle pulses from a mode-locked Cr:ZnS oscillator to drive intra-pulse difference frequency generation in organic nonlinear crystals. The optimized configuration, employing a 200-μm-thick DAST crystal for generation, provided stable and efficient THz pulses from 1 to 39 THz with an efficiency of 0.040%. The system showed excellent long-term stability without deterioration over months of operation and consistency with FTIR measurements.

Optics EXPRESS

Broadband absorption spectroscopy of ZnTe, PE, and PTFE films via EOS with a 100-μm-thick GaP or a 50-μm-thick ZnTe detector further confirmed the capability of this platform to resolve distinct intra- and intermolecular vibrational resonances across the full 1–30 THz range.

Importantly, only a few nanojoules of pump energy were required, highlighting the efficiency of the scheme. The signal-to-noise ratio could be further improved by increasing the gate-pulse power and the scan speed, as it would be possible in a dual-oscillator approach [20]. Together with previous work on ZGP-based MIR continuum generation [17], the present results demonstrate a clear path toward a single-cycle Cr:ZnS oscillator-based spectroscopic system covering the full 1–100 THz range.

Funding. National Research, Development and Innovation Office (2020-2.1.1-ED-2022-00213); Center for Molecular Fingerprinting Research Nonprofit LLC; Japan Science and Technology Agency (JPMJPR24L5); German Academic Exchange Service (JPJSBP120253506); Centre for Advanced Laser Applications; Max Planck Institute of Quantum Optics; Bavarian State Ministry for Science and Art.

Acknowledgment. D. O. acknowledges support from JST PRESTO, Japan, Grant Number JPMJPR24L5. A. W. acknowledges support by the Ministry of Culture and Innovation of Hungary from the National Research, Development and Innovation Fund under the 2020-2.1.1-ED funding scheme. D. O. and A.W. acknowledge Łukasz Sterczewski (Wrocław University of Science and Technology) for discussions on terahertz generation using organic crystals. We gratefully acknowledge support by the Bavarian State Ministry of Science and the Arts in the framework of the project "Empowering Early Intervention: Ultrafast Laser Technology in the Frontier of Cancer Detection". This work was supported by the Center for Molecular Fingerprinting Research Nonprofit LLC (CMF), the Center for Advanced Laser Applications (CALA) at LMU Munich, and the Max Planck Institute of Quantum Optics (MPQ).

Disclosures. The authors declare no conflicts of interest.

Data availability. Data underlying the results presented in this paper are not publicly available at this time but may be obtained from the authors upon reasonable request.

Supplemental document. See Supplement 1 for supporting content.

References

1. E. Gray, H. J. Butler, R. Board, *et al.*, "Health economic evaluation of a serum-based blood test for brain tumour diagnosis: exploration of two clinical scenarios," BMJ Open **8**(5), e017593 (2018).
2. M. Huber, K. V. Kepesidis, L. Voronina, *et al.*, "Stability of person-specific blood-based infrared molecular fingerprints opens up prospects for health monitoring," Nat. Commun. **12**(1), 1511 (2021).
3. T. Eissa, C. Leonardo, K. V. Kepesidis, *et al.*, "Plasma infrared fingerprinting with machine learning enables single-measurement multi-phenotype health screening," Cell Reports Medicine **5**(7), 101625 (2024).
4. K. V. Kepesidis, P. Jacob, W. Schweinberger, *et al.*, "Electric-field molecular fingerprinting to probe cancer," ACS Cent. Sci. **11**(4), 560–573 (2025).
5. B. Ferguson and X.-C. Zhang, "Materials for terahertz science and technology," Nat. Mater. **1**(1), 26–33 (2002).
6. M. Tonouchi, "Cutting-edge terahertz technology," Nat. Photonics **1**(2), 97–105 (2007).
7. L. Yang, T. Guo, X. Zhang, *et al.*, "Toxic chemical compound detection by terahertz spectroscopy: a review," Rev. Anal. Chem. **37**(3), 20170021 (2018).
8. T. P. Butler, N. Lilienfein, J. Xu, *et al.*, "Multi-octave spanning, Watt-level ultrafast mid-infrared source," J. Phys.: Photonics **1**, 044006 (2019).
9. I. Pupeza, M. Huber, M. Trubetskov, *et al.*, "Field-resolved infrared spectroscopy of biological systems," Nature **577**(7788), 52–59 (2020).
10. I. T. Sorokina and E. Sorokin, "Femtosecond Cr^{2+}-based lasers," IEEE J. Sel. Top. Quantum Electron. **21**(1), 273–291 (2015).
11. S. Vasilyev, I. Moskalev, M. Mirov, *et al.*, "Three optical cycle mid-IR Kerr-lens mode-locked polycrystalline Cr^{2+}:ZnS laser," Opt. Lett. **40**(21), 5054–5057 (2015).
12. Y. Wang, T. T. Fernandez, N. Coluccelli, *et al.*, "47-fs Kerr-lens mode-locked Cr:ZnSe laser with high spectral purity," Opt. Express **25**(21), 25193–25200 (2017).
13. N. Nagl, S. Gröbmeyer, V. Pervak, *et al.*, "Directly diode-pumped, Kerr-lens mode-locked, few-cycle Cr:ZnSe oscillator," Opt. Express **27**(17), 24445–24454 (2019).
14. D. Okazaki, H. Arai, A. Anisimov, *et al.*, "Self-starting mode-locked Cr:ZnS laser using single-walled carbon nanotubes with resonant absorption at 2.4 μm," Opt. Lett. **44**(7), 1750–1753 (2019).
15. M. Kowalczyk, I. Davydenko, and J. Sotor, "SESAM-assisted Kerr-lens mode-locked Cr:ZnS laser," Opt. Lett. **49**(18), 5184–5187 (2024).
16. J. M. Pereira, C. Pedersen, and A. Barh, "Diode-pumped gigahertz modelocked Cr:ZnS laser at 2.36 μm," Opt. Lett. **50**(9), 2958–2961 (2025).

Optics EXPRESS

17. P. Steinleitner, N. Nagl, M. Kowalczyk, *et al.*, "Single-cycle infrared waveform control," Nat. Photonics **16**(7), 512–518 (2022).
18. D. Konnov, A. Muraviev, S. Vasilyev, *et al.*, "High-resolution frequency-comb spectroscopy with electro-optic sampling and instantaneous octave-wide coverage across mid-IR to THz at a video rate," APL Photonics **8**(11), 110801 (2023).
19. D. M. B. Lesko, H. Timmers, S. Xing, *et al.*, "A six-octave optical frequency comb from a scalable few-cycle erbium fibre laser," Nat. Photonics **15**(4), 281–286 (2021).
20. A. Weigel, P. Jacob, W. Schweinberger, *et al.*, "Dual-oscillator infrared electro-optic sampling with attosecond precision," Optica **11**(5), 726–735 (2024).
21. A. H. Ohrt, S. Zhou, L. Cheng, *et al.*, "Scanning-free solid-state biased THz waveform detection from 1 to 30 THz," Ultrafast Sci. **5**, 0089 (2025).
22. F. D'Angelo, Z. Mics, M. Bonn, *et al.*, "Ultra-broadband THz time-domain spectroscopy of common polymers using THz air photonics," Opt. Express **22**(10), 12475–12485 (2014).
23. T. Satoh, Y. Toya, S. Yamamoto, *et al.*, "Generation of mid- to far-infrared ultrashort pulses in 4-dimethylamino-N-methyl-4-stilbazolium tosylate crystal," J. Opt. Soc. Am. B **27**(12), 2507–2511 (2010).
24. M. Jazbinsek, U. Puc, A. Abina, *et al.*, "Organic crystals for THz photonics," Appl. Sci. **9**(5), 882 (2019).
25. J. A. Fülöp, S. Tzortzakis, and T. Kampfrath, "Laser-driven strong-field terahertz sources," Adv. Opt. Mater. **8**, 1900681 (2019).
26. K. Miyamoto, T. Yamasaki, S. Tsuji, *et al.*, "Ultrawideband and high-resolution terahertz spectroscopy: Structural identification of glucose," Photonics **9**(9), 602 (2022).
27. S. Mansourzadeh, T. Vogel, A. Omar, *et al.*, "Towards intense ultra-broadband high repetition rate terahertz sources based on organic crystals [invited]," Opt. Mater. Express **13**(11), 3287–3308 (2023).
28. L. A. Sterczewski, J. Mnich, and J. Sotor, "Broadband THz wave generation and detection in organic crystal PNPA at MHz repetition rates," Adv. Phys. Res. **4**(2), 2400105 (2024).
29. Y.-G. Jeong, L. Zanotto, D.-J. Seo, *et al.*, "Multi-microjoule broadband terahertz generation in the organic crystal BNA pumped by ytterbium laser pulses compressed via a gas-filled hollow-core fiber," Opt. Lett. **50**(2), 530–533 (2025).
30. U. Puc, T. Bach, P. Günter, *et al.*, "Ultra-broadband and high-dynamic-range THz time-domain spectroscopy system based on organic crystal emitter and detector in transmission and reflection geometry," Adv. Photonics Res. **2**(4), 2000098 (2021).
31. M. Kowalczyk, N. Nagl, P. Steinleitner, *et al.*, "Ultra-CEP-stable single-cycle pulses at 2.2 μm," Optica **10**(6), 801–811 (2023).
32. N. Nagl, *A New Generation of Ultrafast Oscillators for Mid-Infrared Applications*, Springer Theses (Springer, 2022), 1st ed.
33. D. Hahner, P. Steinleitner, Y. Chen, *et al.*, "Second and third-order dispersion compensating mirror pairs for the spectral range from 1.2-3.2 μm," Opt. Express **30**(21), 38709–38716 (2022).
34. J. Hebling, K.-L. Yeh, M. C. Hoffmann, *et al.*, "Generation of high-power terahertz pulses by tilted-pulse-front excitation and their application possibilities," J. Opt. Soc. Am. B **25**(7), B6–B19 (2008).
35. A. Budweg, D. Yadav, A. Grupp, *et al.*, "Control of excitonic absorption by thickness variation in few-layer GaSe," Phys. Rev. B **100**(4), 045404 (2019).
36. G. Gallot, J. Zhang, R. W. McGowan, *et al.*, "Measurements of the thz absorption and dispersion of ZnTe and their relevance to the electro-optic detection of THz radiation," Appl. Phys. Lett. **74**(23), 3450–3452 (1999).
37. D. T. F. Marple, "Refractive index of ZnSe, ZnTe, and CdTe," J. Appl. Phys. **35**(3), 539–542 (1964).
38. A. Leitenstorfer, S. Hunsche, J. Shah, *et al.*, "Detectors and sources for ultrabroadband electro-optic sampling: Experiment and theory," Appl. Phys. Lett. **74**(11), 1516–1518 (1999).
39. B. R. Steffen, "Electro-optic methods for longitudinal bunch diagnostics at FLASH," Ph.D. thesis, University of Hamburg (2007). DESY-THESIS-2007-020.
40. M. B. Panish and H. C. Casey, "Temperature dependence of the energy gap in GaAs and GaP," J. Appl. Phys. **40**(1), 163–167 (1969).
41. S. Adachi, *Zinc Telluride (ZnTe)* (Springer US, 1999), pp. 473–486.
42. J. Wei, J. M. Murray, J. O. Barnes, *et al.*, "Temperature dependent sellmeier equation for the refractive index of GaP," Opt. Mater. Express **8**(2), 485–490 (2018).
43. M. Nagai, K. Tanaka, H. Ohtake, *et al.*, "Generation and detection of terahertz radiation by electro-optical process in GaAs using 1.56 μm fiber laser pulses," Appl. Phys. Lett. **85**(18), 3974–3976 (2004).
44. E. J. Danielewicz and P. D. Coleman, "Far infrared optical properties of selenium and cadmium telluride," Appl. Opt. **13**(5), 1164–1170 (1974).
45. C.-W. Chen, T.-T. Tang, S.-H. Lin, *et al.*, "Optical properties and potential applications of ϵ-GaSe at terahertz frequencies," J. Opt. Soc. Am. B **26**(9), A58–A65 (2009).
46. T. Skauli, P. S. Kuo, K. L. Vodopyanov, *et al.*, "Improved dispersion relations for GaAs and applications to nonlinear optics," J. Appl. Phys. **94**(10), 6447–6455 (2003).
47. K. Kato, F. Tanno, and N. Umemura, "Sellmeier and thermo-optic dispersion formulas for GaSe (revisited)," Appl. Opt. **52**(11), 2325–2328 (2013).

Optics EXPRESS

48. I. E. Ilyakov, G. K. Kitaeva, B. V. Shishkin, *et al.*, "The use of DSTMS crystal for broadband terahertz electro-optic sampling based on laser pulse amplitude changes," Laser Phys. Lett. **15**(12), 125401 (2018).
49. P. Y. Han, M. Tani, F. Pan, *et al.*, "Use of the organic crystal DAST for terahertz beam applications," Opt. Lett. **25**(9), 675–677 (2000).
50. C.-H. Su, "Energy band gap, intrinsic carrier concentration, and fermi level of CdTe bulk crystal between 304 and 1067 K," J. Appl. Phys. **103**(8), 084903 (2008).
51. S. Casalbuoni, H. Schlarb, B. Schmidt, *et al.*, "Numerical studies on the electro-optic detection of femtosecond electron bunches," Phys. Rev. ST Accel. Beams **11**(7), 072802 (2008).
52. B. Wu, Z. Zhang, L. Cao, *et al.*, "Electro-optic sampling of optical pulses and electron bunches for a compact THz-FEL source," Infrared Phys. Technol. **92**, 287–294 (2018).
53. G. Medvedkin, "Optical dichroism in ZnGeP2 crystals at deep levels," J. Opt. Soc. Am. B **39**(3), 851–858 (2022).
54. D.-G. Xu, X.-L. Zhu, Y.-Y. Wang, *et al.*, "Optical-induced dielectric tunability properties of DAST crystal in THz range," Chin. Phys. B **28**(12), 127701 (2019).
55. S. Krimm, C. Y. Liang, and G. B. B. M. Sutherland, "Infrared spectra of high polymers II: Polyethylene," J. Chem. Phys. **25**(3), 549–562 (1956).
56. G. W. Chantry, J. W. Fleming, E. A. Nicol, *et al.*, "The far infrared spectrum of crystalline polytetrafluoroethylene," Polymer **15**(2), 69–73 (1974).
57. C. Y. Liang and S. Krimm, "Infrared spectra of high polymers III: Polytetrafluoroethylene and polychlorotrifluoroethylene," J. Chem. Phys. **25**(3), 563–571 (1956).